



Supercritical carbon dioxide–brine–rock reactions in the Madison Limestone of Southwest Wyoming: An experimental investigation of a sulfur-rich natural carbon dioxide reservoir

Curtis Chopping^{a,1}, John P. Kaszuba^{a,b,*}

^a Department of Geology and Geophysics, 1000 E. University Avenue, University of Wyoming, Laramie, WY 82071, USA

^b School of Energy Resources, 1000 E. University Avenue, University of Wyoming, Laramie, WY 82071, USA

ARTICLE INFO

Article history:

Received 17 September 2011

Received in revised form 5 June 2012

Accepted 3 July 2012

Available online 11 July 2012

Editor: B. Sherwood-Lollar

Keywords:

Fluid–rock interactions

Carbon dioxide reservoir

Natural analog

Geologic carbon sequestration

Co-sequestration

Supercritical carbon dioxide

ABSTRACT

The Madison Limestone on the Moxa Arch, southwest Wyoming, USA is a sulfur-rich natural CO₂ reservoir. A series of hydrothermal experiments was performed to evaluate multi-phase (CO₂–H₂O)–brine–rock reactions and processes in this reservoir and to test the hypothesis that this reservoir is a natural analog for geologic carbon–sulfur co-sequestration. Idealized Madison Limestone (dolomite–calcite–anhydrite–pyrite) and Na–Cl–SO₄^{2−} brine (I = 0.5 molal) reacted at 110 °C and 25 MPa for approximately 81 days (1940 h). Supercritical CO₂ was then injected and the experiment continued for approximately 46 days (1100 h). A parallel experiment was performed without supercritical CO₂ to provide a basis of understanding for the interaction of supercritical CO₂ with the brine–rock system. Two additional experiments were conducted in the same manner, but without anhydrite in the starting mineral assemblage, to examine supercritical CO₂–sulfur reactivity.

Injection of supercritical CO₂ decreases pH by 2.5 to 3.3 units, increases Eh by 0.19 to 0.23 V, and drives reaction pathways along the pyrite–anhydrite saturation boundary of an Eh–pH diagram. The dolomite–calcite–anhydrite mineral assemblage and reaction textures that are produced are consistent with those observed in the natural CO₂ reservoir. The mineral assemblage does not change following emplacement of supercritical CO₂; instead, minerals dissolve, mobilize and re-precipitate. Anhydrite precipitates in the dolomite–calcite–pyrite experiment following injection of supercritical CO₂ and provides a mineral trap for sulfur. Anhydrite precipitation decreases SO₄^{2−} activity, ultimately leading to mineralization of CO₂. Experimental results support the hypothesis that the Madison Limestone on the Moxa Arch is a natural analog for geologic carbon–sulfur co-sequestration.

© 2012 Elsevier B.V. All rights reserved.

1. Introduction

Carbon dioxide reservoirs occur naturally in the Earth's crust. The advent of geologic carbon sequestration, also known as carbon capture and storage or CCS, has generated scientific interest in these reservoirs. Naturally-occurring carbon dioxide reservoirs are often referred to as natural analogs (Allis et al., 2001). They have stored supercritical carbon dioxide, and in some cases other components such as hydrogen sulfide, for geologic scales of time. Our understanding of geochemical reactions and processes in these supercritical carbon dioxide–brine–rock systems is limited. Improved understanding of these natural systems will help clarify long-term storage behavior of reactive carbon dioxide in anthropogenic systems.

* Corresponding author at: Department of Geology and Geophysics, 1000 E. University Avenue, University of Wyoming, Laramie, WY 82071, USA. Tel.: +1 307 766 6065; fax: +1 307 766 6679.

E-mail addresses: cchopp@uwyo.edu (C. Chopping), John.Kaszuba@uwyo.edu (J.P. Kaszuba).

¹ Present address: Enhanced Oil Recovery Institute, 1000 E. University Avenue, University of Wyoming, Laramie, WY 82071, USA.

Several natural carbon dioxide reservoirs occur on the Colorado Plateau and in the Southern Rocky Mountains of the USA, including Bravo Dome in New Mexico, McElmo Dome and Sheep Mountain in Colorado, Farnham Dome in Utah, the Springerville–St. Johns field in Arizona and New Mexico, and the Moxa Arch in Southwest Wyoming (Pearce et al., 1996; Allis et al., 2001; Stevens et al., 2001; Moore et al., 2005; Gilfillan et al., 2008; Kaszuba et al., 2011). The Moxa Arch is receiving particular scrutiny as a natural analog (Allis et al., 2001; Kaszuba et al., 2011; Lynds et al., 2010; Smith et al., 2010; Thyne et al., 2010). The Moxa Arch is a 200 km long, north–south trending Cretaceous uplift (Kraig et al., 1987) bound by the Laramide Overthrust Belt to the west and by the Rock Springs Uplift to the east (Fig. 1). Several Paleozoic units on the Moxa Arch house natural carbon dioxide reservoirs, including the Bighorn Dolomite, Madison Limestone, Weber Sandstone, and Phosphoria Formation (De Bruin, 1991). Temperatures and pressures in these reservoirs exceed the critical point of carbon dioxide, 31 °C and 7.4 MPa (Span and Wagner, 1996), thus the carbon dioxide is in a supercritical state.

In addition to carbon dioxide, the Madison Limestone on the Moxa Arch contains methane (up to 22 vol.%), nitrogen (up to 7 vol.%),

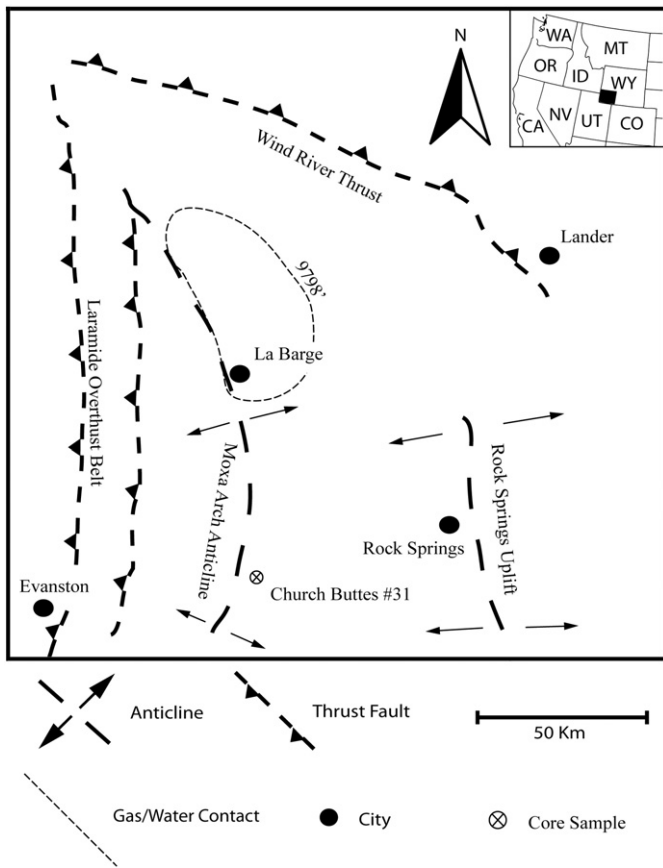


Fig. 1. Modified geologic map of southwestern Wyoming, USA, (Kraig et al., 1987; De Bruin, 1991). Gas/water contact of CO₂ reservoir plotted as thin dashed line (Stilwell, 1989). Location of well where Madison Limestone drill core was sampled (Church Buttes #31) is also plotted.

hydrogen sulfide (up to 4.5 vol.%), and helium (up to 0.5 vol.%) (De Bruin, 1991). Aqueous sulfate and sulfide as well as recrystallized anhydrite (Fig. 2) and pyrite, known products of sulfur dioxide disproportionation in other water–rock systems, are also present (Kaszuba et al., 2011). These characteristics, combined with a thermodynamic analysis, led Kaszuba et al. (2011) to propose this carbon dioxide reservoir as a natural analog for geologic co-sequestration of carbon dioxide and sulfur. Co-sequestration is a strategy for managing carbon dioxide that contains impurities produced by coal combustion, particularly SO_x and NO_x.

The purpose of this study is to: 1) evaluate multi-phase (CO₂–H₂O)–brine–rock reactions and processes in a sulfur-rich natural carbon dioxide reservoir; and 2) test the hypothesis that the Madison Limestone on the Moxa Arch is a natural analog for geologic carbon–sulfur co-sequestration. We perform an experimental evaluation of interactions among supercritical carbon dioxide, brine, and idealized Madison Limestone to accomplish these two goals. Mineral textures and geochemical features that developed in the experiments suggest that the carbonate rock which constitutes the natural reservoir will initially dissolve in response to injected supercritical carbon dioxide but will re-precipitate with its constituent minerals as the rock reasserts geochemical control. Anhydrite precipitates in the experiments in response to injected carbon dioxide, suggesting that secondary anhydrite precipitation in the natural reservoir (Fig. 2) may be related to emplacement of carbon dioxide into the Madison Limestone. From these results a number of clear implications are drawn regarding multi-phase fluid–rock interactions in a natural carbon dioxide reservoir and the suitability of the Madison Limestone on the Moxa Arch as a natural analog for carbon–sulfur co-sequestration. While experimental laboratory studies have long been used to evaluate geochemical aspects of proposed

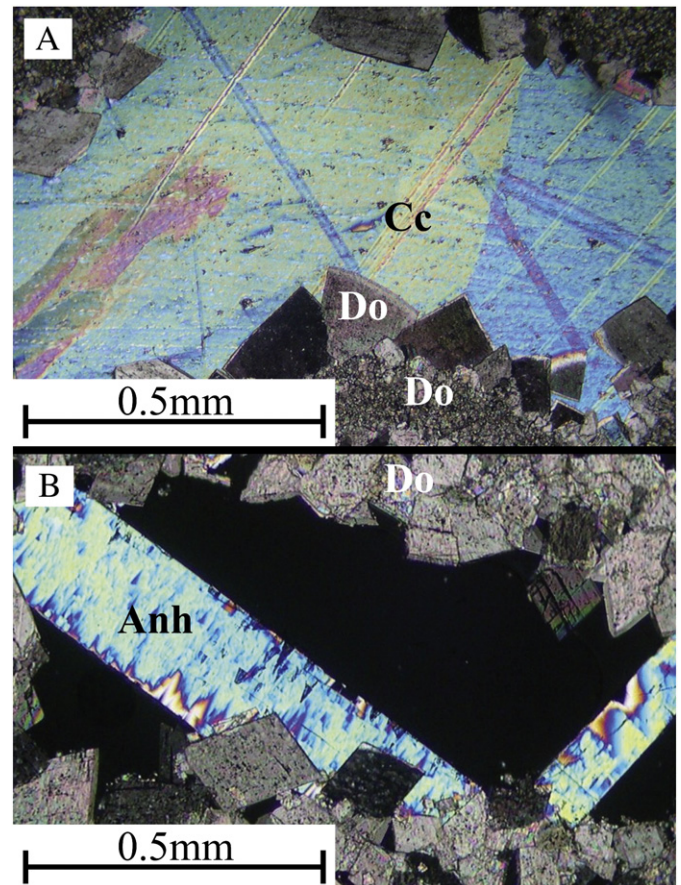


Fig. 2. Photomicrographs of Madison Limestone core obtained from Church Buttes #31 at depths of 18,340 and 18,706 ft, respectively (Fig. 1). Scale bar is 0.5 mm in both images. A) The matrix is composed of disseminated dolomite (Do). Rhombohedral secondary dolomite containing iron rich rims as well as secondary calcite (Cc) fills the pore in the center of the image. B) Secondary dolomite rhombohedrons and secondary anhydrite (Anh) fill the pore in the center of the image.

anthropogenic carbon storage reservoirs (e.g., Pearce et al., 1996; Gunter et al., 1997), to our knowledge this is the first experimental study published in the scientific literature that evaluates multi-phase (CO₂–H₂O)–fluid–rock interactions relevant to a natural carbon dioxide reservoir. Employing geochemical laboratory experiments to understand natural carbon dioxide reservoirs helps to elucidate the reactions and processes that take place during evolution of the natural system. In turn, natural carbon dioxide reservoirs provide important constraints on the design and interpretation of laboratory experiments that emulate both natural and anthropogenic systems.

2. Methods and materials

2.1. Approach

Our approach was to conduct a series of experiments that evaluates reactions and processes among supercritical carbon dioxide, brine, and a carbonate reservoir at conditions comparable to those of the Madison Limestone in Southwest Wyoming. The Madison Limestone in Southwest Wyoming is actually a dolostone that contains dolomite, calcite, anhydrite (Fig. 2) and pyrite as well as accessory silicate minerals (quartz ± feldspar ± analcime ± illite) and native sulfur (Kaszuba et al., 2011). To simplify our analysis, the experiments presented in this paper contained only the major minerals found in the Madison Limestone (dolomite, calcite, anhydrite and pyrite) and not the accessory silicate minerals or native sulfur. Future experiments will address the additional complexities

that these accessory minerals pose. The experiments were performed at 110 °C, reservoir temperatures found in the Madison Limestone on the Moxa Arch.

In the first experiment, brine and idealized Madison Limestone (dolomite, calcite, anhydrite, and pyrite) reacted at 110 °C and 25 MPa for approximately 81 days (1940 h). Carbon dioxide was then injected into the system and the experiment continued for approximately 46 days (1100 h) (Table 1). At 110 °C and 25 MPa, carbon dioxide is a supercritical fluid that freely reacts with the carbonate reservoir–brine system. Excess carbon dioxide was injected to ensure that two immiscible fluid phases (Takenouchi and Kennedy, 1964; Shyu et al., 1997; Duan et al., 2006), a constant carbon dioxide fugacity, and carbon dioxide saturation of brine existed for the duration of the experiment. Injection of carbon dioxide increases pressure in direct proportion to the mass of supercritical carbon dioxide added to the experiment. Carbon dioxide was injected in two stages and pressure was manually decreased during an intervening stage to ensure that a sufficient mass of carbon dioxide was injected without exceeding pressure limitations of the experimental apparatus. In these closed-system experiments, pressure subsequently decreased due to dissolution of supercritical carbon dioxide into brine. Steady state pressure was achieved within 24 h. Pressure was subsequently decreased and maintained at 25 MPa once fluid sampling began.

A second experiment was performed to provide a basis of understanding for the interaction of supercritical carbon dioxide with the brine–rock system. In this experiment, brine and rock reacted for approximately 95 days (2280 h) at 110 °C and 25 MPa and without injection of carbon dioxide (Table 1).

With the understanding afforded by these two experiments we conducted two additional experiments to test the hypothesis that the Madison Limestone is a natural analog for carbon–sulfur co-sequestration. For these two additional experiments we assume that the co-injected sulfur is sulfur dioxide, the most abundant constituent in SO_x and a very reactive compound in water–rock systems. We further assume that the sulfur dioxide has already dissolved into the brine–rock system and reacted to form sulfate, one of the ultimate end products of sulfur dioxide disproportionation (Holland, 1965; Getahun et al., 1996; Symonds et al., 2001). Thus our approach examines supercritical carbon dioxide–sulfur reactivity in a sulfate brine–rock system. We do not evaluate reaction pathways of co-injected

sulfur dioxide. Evaluating these complexities will require additional experiments and is beyond the scope of this investigation.

This second pair of experiments contained dolomite, calcite, and pyrite but no anhydrite. In all other respects, including brine composition, temperature, and pressure, this pair of experiments was conducted in the same manner as the first two experiments. With this approach we have changed one variable, the presence or absence of anhydrite. In one experiment, brine and rock reacted for approximately 69 days (1650 h). Carbon dioxide was then injected into the system and the experiment continued for approximately 45 days (1080 h). In a companion experiment, brine and rock reacted for approximately 95 days (2280 h) and without injection of carbon dioxide (Table 1).

2.2. Experimental apparatus and procedure

The experiments were conducted in a rocking autoclave, also known as a rocker bomb, using established methods for hydrothermal experiments (Seyfried et al., 1987). This equipment allows external control and monitoring of temperature and pressure. Experimental temperature and pressure were reached in an average of 5.8 h. Estimated maximum temperature and pressure uncertainty is ± 1 °C and ± 0.6 MPa, respectively (Table 1).

Our hydrothermal apparatus was equipped with a Dickson-type reaction cell consisting of a flexible 150 cm³ titanium reaction cell, head, and capillary tube ported with a metered sampling valve. Brine samples were periodically withdrawn on a logarithmic time scale from the reaction cell without perturbing the ongoing experiment. Samples were rapidly cooled and depressurized to ambient conditions in a few seconds and subsequently analyzed. Retrograde reactions with minerals that may occur during a prolonged quench process were consequently avoided and solution composition was analyzed along a reaction pathway. The minerals and quenched brine were also analyzed after the experiments were terminated. Carbon dioxide was introduced into the reaction cell for two of the experiments using a Teledyne-ISCO 260D syringe pump. This procedure is consistent with previous investigations that evaluate supercritical carbon dioxide–water–rock reactions using rocking autoclaves (Kaszuba et al., 2003; Kaszuba et al., 2005; Palandri and Kharaka, 2005; Rosenbauer et al., 2005).

Table 1
Mineral composition and experimental parameters.

Elemental weight percent (wt.% oxide)				
Component ^a	Dolomite (Do)	Calcite (Cc)	Anhydrite (Anh)	Pyrite (Py)
CaO	31.4	57.4	41.1	–
MgO	17.0	0.1	–	–
FeO	6.7	–	–	60.0
MnO	0.2	–	–	–
Surface area (m ² /g) ^b	0.539 ± 0.010	0.792 ± 0.021	0.945 ± 0.010	Not available
Description	Wards Scientific #49 E 5871	Wards Scientific #49-5860	Wards Scientific (no number)	Wards Scientific #49-5884
Source	Selasvann, Norway	Zacatecas, Mexico	Naica, Mexico	Santa Eulalia, Mexico
Experiment ^c	Do–Cc–Anh–Py + brine + scCO ₂	Do–Cc–Anh–Py + brine	Do–Cc–Py + brine + scCO ₂	Do–Cc–Py + brine
Temperature (°C)	110 ± 0.4	110 ± 1.0	110 ± 0.8	110 ± 0.3
Pressure (MPa)	25 ± 0.5	25 ± 0.6	25 ± 0.5	25 ± 0.5
Water/rock ratio ^d	31.4:1	32.7:1	31.1:1	30.1:1
Mineral proportions (wt.% mass) ^e	82.6, 10.0, 6.0, 1.4	82.6, 9.8, 6.0, 1.6	85.7, 13.3, 1.0	85.8, 13.2, 1.0
Brine–rock reaction time (hours) ^f	3040	2280	2730	2280
Brine–rock + supercritical CO ₂ (hours) ^g	1100	na	1080	na

na = not applicable.

^a Ca, Mg, Fe, Mn measured by ICP-OES after acid digestion of the mineral. Minerals were also analyzed using optical microscopy, high-resolution field emission scanning electron microscopy (FE-SEM), energy dispersive spectra (EDS), X-ray diffraction (XRD), and BET surface area analyses.

^b Surface areas measured using BET.

^c Minerals and fluids used in experiments, scCO₂ = supercritical carbon dioxide.

^d Mass of brine to 5 g of minerals used in experiments.

^e Proportion of minerals used in experiments, combined to a total of 5 g.

^f Total amount of reaction time between brine and rock in brine–rock experiment or in scCO₂–brine–rock experiment before injection of scCO₂.

^g Total amount of reaction time after addition of scCO₂.

2.3. Materials

The surrogate Madison Limestone constructed for the first pair of experiments consisted of 83 wt.% dolomite (Do), 10 wt.% calcite (Cc), 6 wt.% anhydrite (Anh), and 1 wt.% pyrite (Py) (Table 1). This mixture is consistent with the mineralogy of the Madison Limestone on the Moxa Arch (Budai et al., 1987; Kaszuba et al., 2011). Madison Limestone in the second pair of experiments consisted of 86 wt.% dolomite, 13 wt.% calcite, and 1 wt.% pyrite. Instead of using an actual sample of Madison Limestone, research-grade dolomite, calcite, anhydrite, and pyrite of known origin were combined in the appropriate proportions (Table 1). This approach reduced the possibility of preexisting alteration minerals being introduced into the experiment and ensured the precise proportion and composition of constituent minerals.

Mineral fragments and powders were used in each experiment. Use of mineral fragments promoted recovery of minerals of sufficient size that reaction textures could be evaluated. Use of mineral powders enhanced reactivity and maximized reaction rates. Mineral fragments were 0.5 to 3.0 mm in size. Mineral powders were prepared by grinding in a ceramic mortar and pestle and sieving with a 45 µm sieve. BET surface areas for these mineral powders are presented in Table 1. Approximately 5 g of minerals (75 wt.% fragments and 25 wt.% powders) and approximately 150 g of synthetic brine were used in each experiment (Table 1).

A synthetic brine (initial brine entry in Tables 2 and 3) was prepared using laboratory-grade salts. Nanopure water (18 Ω) was

sparged with argon gas prior to synthesis in order to remove dissolved gasses, particularly dissolved oxygen and carbon dioxide. The bulk composition and ionic strength (0.5 m) of the brine are consistent with available analyses of Madison Limestone formation waters as compiled by Kaszuba et al. (2011) from the USGS Produced Waters Database (Breit and Skinner, 2002) and the Wyoming Oil and Gas Conservation Commission website (Wyoming Oil and Gas Conservation Commission, 2009).

To minimize mineral reaction with the brine before injection of carbon dioxide, the major element composition of the brine was formulated to be saturated with dolomite, calcite, anhydrite, and pyrite at experimental conditions. Since the fluid geochemistry is controlled by the minerals, the experiments are a rock-dominated system until carbon dioxide is injected. Thus the brine contained calcium, magnesium, and bicarbonate in concentrations determined by equilibrium with dolomite and calcite. The brine also contained calcium and sulfate in concentrations determined by equilibrium with calcite and anhydrite. Quantities of iron required to bring the fluid into equilibrium with pyrite are exceedingly small and difficult to measure accurately. Therefore, the brine was synthesized without iron. Sodium and chloride were added to achieve the desired ionic strength. Despite these efforts, the brine was not perfectly saturated with the minerals in each experiment. Lack of equilibrium was due to solid solution in the minerals and weighing errors incurred during brine synthesis. Each experiment reacted minerals and brine before the addition of supercritical carbon dioxide to approach a steady state to the extent possible.

Table 2
Water chemistry results (mmol/kg) for brine-Do-Cc-Anh-Py±scCO₂ experiment, 110 °C, 25 MPa.

Time (hours)	pH (STP) ^a	pH (in-situ) ^b	Cl	SO ₄	Na	Ca	Mg	Mn	Fe	SiO ₂ (aq)	Cu	Sr	ΣCO ₂	Charge balance
<i>Water chemistry (mmol/kg), synthetic brine-Do-Cc-Anh-Py-scCO₂, 110 °C, 25 MPa</i>														
Initial brine ^c	9.8	na	316.9	79.7	488.5	0.4	1.1	<0.00005	<0.00004	<0.001	0.01	0.01	2.7	2.7%
31	7.3	7.3	339.9	89.1	524.3	2.9	1.2	<0.00005	<0.00004	0.07	0.01	0.02	0.6	2.5%
53	7.6	7.3	368.4	95.5	589.1	3.6	1.3	<0.00005	<0.00004	0.11	0.01	0.02	1.2	4.4%
126	7.6	7.4	345.6	90.2	543.8	3.8	1.2	<0.00005	<0.00004	0.09	0.00	0.02	1.7	3.6%
367 ^d	7.8	7.3	410.7	106.5	640.6	5.7	1.5	<0.00005	<0.00004	0.13	0.01	0.03	1.1	3.5%
1945	7.4	7.3	378.0	99.5	492.6	4.6	1.1	<0.00005	<0.00004	0.11	0.04	0.02	1.4	−6.8%
<i>Inject CO₂ at 1949</i>														
1974	6.4	4.8	341.3	78.1	561.5	12.0	5.5	0.04	0.06	0.35	0.02	0.01	1037.7	9.2%
1997	6.4	4.8	362.8	78.5	544.0	10.9	5.3	0.04	0.05	0.43	0.01	0.01	1129.3	5.3%
2181	6.5	4.8	346.6	62.8	481.9	6.1	4.9	0.05	0.07	0.43	0.01	0.01	1148.4	3.5%
2546 ^d	6.6	4.8	438.3	69.0	748.5	9.8	8.5	0.07	0.16	0.81	0.03	0.01	1163.3	−4.1%
3025	6.7	4.9	310.4	45.7	488.5	5.3	4.7	0.03	0.09	0.50	0.01	0.01	1108.7	12.0%
<i>Quench^e at 3057</i>														
Quench ^e at 3057	8.7	na	328.4	53.2	482.1	9.5	4.8	0.02	0.02	0.46	0.01	0.01	66.3	8.2%
Uncertainty	±0.1	±0.1	±1.8	±0.7	±27.9	±0.1	±0.1	±0.01	±0.01	±0.01	±0.01	±0.01	±6%	na
Predicted equilibrium values ^f		5.2	377	43	500	5.0	1.2	<0.00005	0.002	0.05	0.01	0.01	1100	na
<i>Water chemistry (mmol/kg), synthetic brine-Do-Cc-Anh-Py, 110 °C, 25 MPa</i>														
Initial brine ^c	8.6	na	317.9	79.6	461.7	0.4	1.0	<0.00005	<0.00004	<0.001	0.01	0.01	2.6	−1.6%
25	7.8	7.5	312.6	80.5	464.5	2.4	1.1	<0.00005	<0.00004	0.05	0.01	0.01	1.9	−0.4%
49	7.8	7.5	310.9	81.1	458.4	2.8	1.1	<0.00005	<0.00004	0.07	0.01	0.02	2.1	−0.9%
122	7.6	7.4	308.4	81.5	468.9	3.6	1.1	<0.00005	<0.00004	0.06	0.01	0.02	2.0	0.5%
409	7.3	7.2	308.5	82.3	484.6	4.2	1.1	<0.00005	<0.00004	0.07	0.01	0.02	1.1	2.2%
1080	7.4	7.3	301.5	80.5	455.4	4.2	1.1	<0.00005	<0.00004	0.10	0.01	0.02	1.7	0.2%
2280	7.4	7.3	322.8	81.3	457.8	4.3	1.1	<0.00005	<0.00004	0.11	0.01	0.02	2.2	−1.8%
<i>Quench^e at 2282</i>														
Quench ^e at 2282	7.8	na	314.7	80.1	469.8	4.5	1.1	<0.00005	<0.00004	0.10	0.01	0.02	2.3	0.5%
Uncertainty	±0.1	±0.1	±1.8	±0.7	±27.9	±0.1	±0.1	±0.01	±0.01	±0.01	±0.01	±0.01	±4%	na
Predicted equilibrium values ^f		7.3	337	84	500	2.5	0.8	<0.00005	0.001	0.05	0.01	0.01	1.4	na

Dissolved major cations (Na, Ca, Mg, SiO₂, Fe and Mn) were determined by inductively coupled plasma optical emission spectroscopy (ICP-OES), dissolved minor cations (Cu and Sr) by inductively coupled plasma mass spectroscopy (ICP-MS), and dissolved anions (Cl and SO₄) by ion chromatography.

na = not applicable.

^a Standard room pressure (0.1 MPa) and temperature (25 °C).

^b Calculated value, see Section 2.5 for explanation of methods.

^c Composition of unreacted brine.

^d Evaporative losses, refer to Fig. 3A and B for magnitude of error due to these losses.

^e Composition of brine after experiment is terminated.

^f See Section 2.5 for explanation of methods.

Table 3Water chemistry results (mmol/kg) for brine-Do-Cc-Py±scCO₂ experiment, 110 °C, 25 MPa.

Time (hours)	pH (STP) ^a	pH (in-situ) ^b	Cl	SO ₄	Na	Ca	Mg	Mn	Fe	SiO ₂ (aq)	Cu	Sr	ΣCO ₂	Charge balance
<i>Water chemistry (mmol/kg), synthetic brine-Do-Cc-Py-scCO₂, 110 °C, 25 MPa</i>														
Initial brine ^c	9.6	na	345.4	85.7	512.7	0.4	1.2	<0.00005	<0.00004	0.02	0.01	0.01	1.9	-0.3%
26	7.5	7.4	383.3	94.4	539.1	0.3	0.9	<0.00005	<0.00004	0.04	0.01	0.01	1.8	-2.9%
51	8.8	8.0	357.9	89.2	520.0	0.3	1.0	<0.00005	<0.00004	0.06	0.01	0.01	1.9	-1.4%
121	8.8	8.0	342.4	86.5	510.5	0.3	0.6	<0.00005	<0.00004	0.04	0.01	0.01	1.1	-0.4%
359	8.6	7.8	345.9	85.8	535.9	0.5	0.5	<0.00005	<0.00004	0.04	0.01	0.01	1.5	1.8%
1653	8.8	7.9	329.2	81.9	492.6	0.6	0.3	<0.00005	<0.00004	0.06	0.01	0.01	0.8	0.1%
<i>Inject CO₂ at 1657</i>														
1682	6.3	4.6	325.4	76.3	513.3	11.7	5.0	0.04	0.02	0.28	0.01	0.01	1241.4	6.8%
1706 ^d	6.4	4.7	398.5	89.5	516.3	11.6	5.1	0.05	0.03	0.31	0.01	0.01	1110.3	-2.3%
1869	6.4	4.7	352.7	72.3	551.9	11.0	5.5	0.06	0.03	0.45	0.01	0.01	1168.7	8.3%
2212	6.6	4.7	361.0	62.3	498.2	6.3	5.1	0.06	0.06	0.45	0.01	0.00	1215.2	3.7%
2686 ^d	6.6	4.8	310.5	47.4	532.9	6.4	5.5	0.05	0.06	0.49	0.01	0.00	1170.9	15.9%
<i>Quench^e at 2737</i>														
Quench ^e at 2737	8.8	na	313.6	50.9	486.7	7.2	4.8	0.02	0.01	0.45	0.01	0.00	54.0	10.5%
Uncertainty	±0.1	±0.1	±1.8	±0.7	±27.9	±0.1	±0.1	±0.01	±0.01	±0.01	±0.01	±0.01	±6%	na
Predicted equilibrium values ^f		5.2	337	41	500	5.2	1.0	<0.00005	0.002	0.05	0.01	0.01	1100	na
<i>Water chemistry (mmol/kg), synthetic brine, Do-Cc-Py, 110 °C, 25 MPa</i>														
Initial brine ^c	8.9	na	321.5	80.5	461.9	0.4	1.0	<0.00005	<0.00004	<0.001	0.01	0.01	2.3	-2.1%
24	8.5	7.9	311.0	78.5	462.1	0.5	0.8	<0.00005	<0.00004	0.05	0.01	0.01	2.1	-0.6%
49	8.3	7.8	308.6	76.0	441.9	0.5	0.8	<0.00005	<0.00004	0.07	0.01	0.01	2.7	-2.0%
121	8.4	7.8	297.3	75.4	453.5	0.6	0.7	<0.00005	<0.00004	0.09	0.02	0.01	1.9	0.7%
408	8.4	7.7	290.2	73.8	437.2	0.8	0.5	<0.00005	<0.00004	0.17	0.02	0.01	1.1	0.2%
1080	8.2	7.6	287.5	72.6	451.3	0.9	0.4	<0.00005	<0.00004	0.31	0.01	0.01	1.5	2.4%
2280	8.2	7.7	293.9	72.4	440.0	1.0	0.4	<0.00005	<0.00004	0.50	0.01	0.01	2.7	0.4%
<i>Quench^e 2283</i>														
Quench ^e 2283	8.3	na	283.2	69.1	444.3	1.1	0.4	<0.00005	<0.00004	0.52	0.01	0.01	2.6	2.9%
Uncertainty	±0.1	±0.1	±1.8	±0.7	±27.9	±0.1	±0.1	±0.01	±0.01	±0.01	±0.01	±0.01	±4%	na
Predicted equilibrium values ^f		7.7	337	82	500	0.9	0.3	<0.00005	0.001	0.05	0.01	0.01	1.6	na

Dissolved major cations (Na, Ca, Mg, SiO₂, Fe and Mn) were determined by inductively coupled plasma optical emission spectroscopy (ICP-OES), dissolved minor cations (Cu and Sr) by inductively coupled plasma mass spectroscopy (ICP-MS), and dissolved anions (Cl and SO₄) by ion chromatography.

na = not applicable.

^a Standard room pressure (0.1 MPa) and temperature (25 °C).

^b Calculated value, see Section 2.5 for explanation of methods.

^c Composition of unreacted brine.

^d Evaporative losses, refer to Fig. 3A and B for magnitude of error due to these losses.

^e Composition of brine after experiment is terminated.

^f See Section 2.5 for explanation of methods.

2.4. Analytical methods

Analytical methods and results for brine samples, including charge balance and analytical uncertainties, are reported in Table 2 (Do-Cc-Anh-Py experiments) and Table 3 (Do-Cc-Py experiments). Analytical results are also plotted in Figs. 3 and 4. A titanium filter installed in the head of the reaction cell filtered the brine samples. To prevent mineral precipitation, the samples for cation analysis were acidified to pH 2 using trace metal grade nitric acid. Mineral precipitants were not observed in any of the brine samples.

The pH was not measured at in-situ temperature and pressure. Instead, “benchtop” pH was determined using an Orion pH meter and Ross microelectrode on degassed brine samples cooled to 25 °C and depressurized to 0.1 MPa. Total dissolved inorganic carbon (as carbon dioxide) was also determined on these degassed and cooled brine samples. The analysis was performed using coulometric titration (Huffmann, 1977). In-situ values of total dissolved inorganic carbon were determined by analyzing a sample of brine collected in a glass gas-tight syringe. The syringe contains carbon dioxide dissolved in brine as well as carbon dioxide that exsolved due to the reduced pressure and temperature of ambient conditions. These pH and dissolved inorganic carbon values were used to calculate in-situ pH (Section 2.5).

2.5. Geochemical calculations

Geochemical calculations were performed using The Geochemist's Workbench® version 8.0.10 (Bethke and Yeakel, 2009), the b-dot ion

association model, and the resident thermodynamic database thermo.com.V8.R6+.dat. Thermo.com.V8.R6+.dat was chosen because it contains the most comprehensive data compilation for relevant sulfur minerals, aqueous complexes and gasses. Thermodynamic data for dolomite was adjusted using an ideal solution model to improve the ability of the calculations to account for the nonstoichiometric dolomite used in these experiments.

Two kinds of geochemical calculations were performed. First, forward models were calculated to determine the final equilibrium state to which each of the four experiments would theoretically evolve. Each of these four calculations was constrained by the composition of the synthetic brine (initial brine entry in Tables 2 and 3) and the amount of each of the minerals used in the experiment. Equilibrium concentrations of carbon dioxide in the two brine-rock experiments that are not reacted with supercritical carbon dioxide are constrained by equilibrating minerals with brine at experimental conditions. An equation of state such as the one proposed by Duan et al. (2006) cannot be used to constrain these calculations because the brine is not saturated with carbon dioxide. However, since the two experiments reacted with supercritical carbon dioxide contained excess supercritical carbon dioxide throughout their duration, the theoretical solubility of carbon dioxide in these experiments was constrained using the equation of state of Duan et al. (2006). The theoretical predictions provided by our forward models are plotted in the panel labeled “p” in Figs. 3 and 4 and listed in Tables 2 and 3. We discuss these predictions relative to our experimental results in Section 3 (Results).

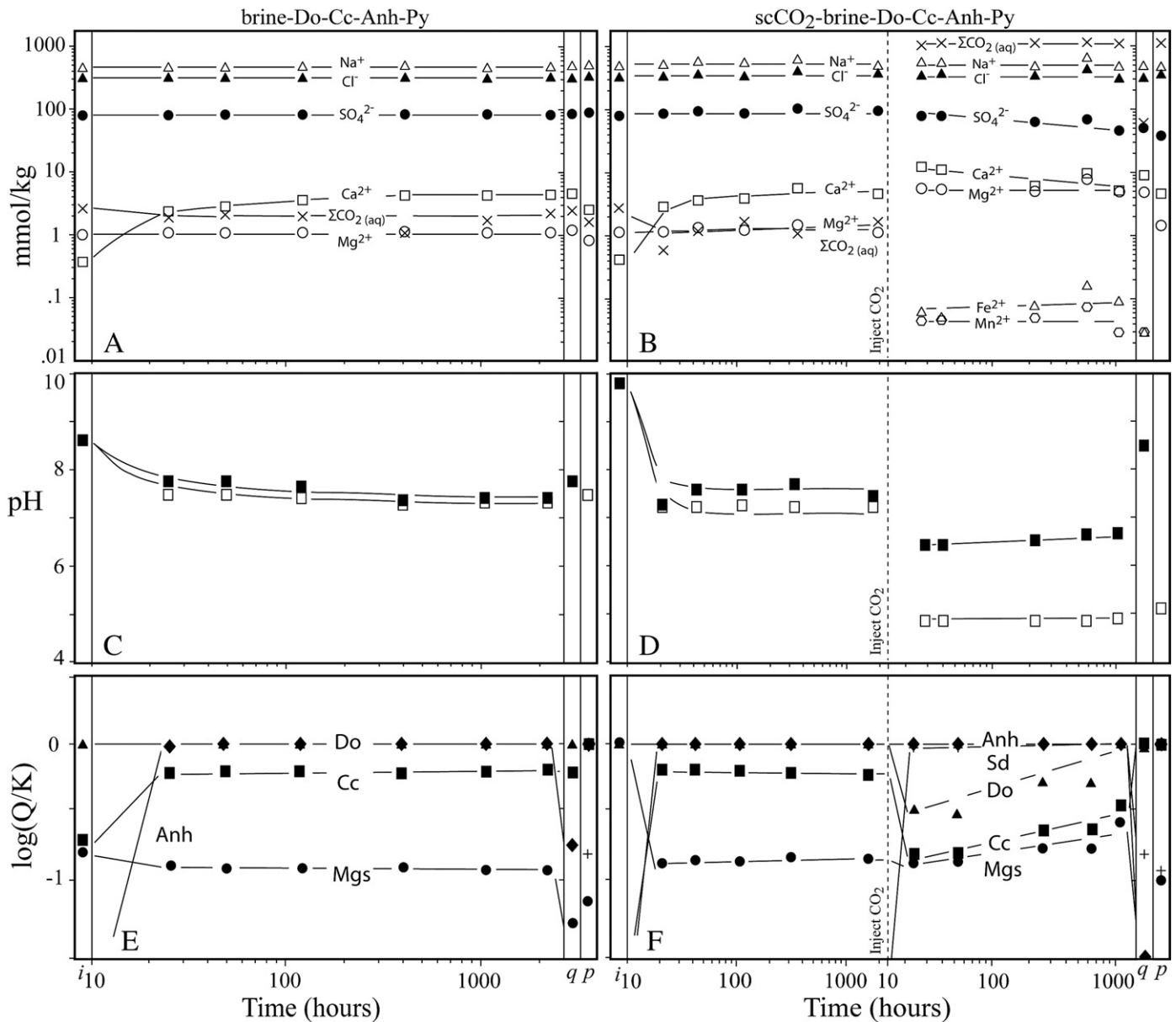


Fig. 3. Geochemistry of brine as a function of log time for the brine–dolomite (Do)–calcite (Cc)–anhydrite (Anh)–pyrite (Py) experiment (graphs in column on the left) and the supercritical carbon dioxide (scCO₂)–brine–Do–Cc–Anh–Py experiment (graphs in column on the right). A) and B) Log concentration of Na (triangle), Ca (square), Mg (circle), Fe (triangle), Mn (hexagon), Cl (filled triangle), SO₄ (filled circle), and ΣCO₂ (‘x’); C) and D) benchtop pH (filled square) and calculated in-situ pH (square); and E) and F) calculated saturation states of the minerals anhydrite (filled diamond), dolomite (filled triangle), calcite (filled square), siderite (Sd, crosses), and magnesite (Mgs, filled circles). Each graph also depicts the geochemistry of unreacted brine at 25 °C, 0.1 MPa (panel labeled *i*); the geochemistry of the brine at 25 °C, 0.1 MPa after termination of the experiment (panel labeled *q*); and the predicted equilibrium state of the brine at 110 °C, 25 MPa (panel labeled *p*) based upon reaction path calculations using Geochemist Workbench 8.0.1 (Bethke and Yeakel, 2009).

The second type of calculation evaluates the geochemistry of individual samples collected from each experiment. These calculations determine in-situ pH (Section 3.3), saturation state (Section 3.4), and activities of aqueous species and minerals in reacted brine. Activity data were used to determine geochemical reaction paths (Section 4.2) for each of the four experiments. In-situ pH for samples of brine that did not react with supercritical carbon dioxide was determined by speciating the fluid at 110 °C. In-situ pH for samples of brine that reacted with supercritical carbon dioxide was determined using the method of Newell et al. (2008). This method uses “benchtop” pH and dissolved inorganic carbon, the chemical analysis, and in-situ dissolved inorganic carbon (Section 2.4) to calculate in-situ pH.

Ions present in concentrations of less than 0.01 mmolal were not used in the calculations. For saturation state calculations we explicitly included minerals used in our experiments (dolomite, calcite, anhydrite,

and pyrite), minerals observed to precipitate in similar experiments or in geochemical simulations of carbon reservoirs (siderite and magnesite), and minerals observed in the Madison Limestone (native sulfur).

3. Results

3.1. Major and minor elements in brine

3.1.1. Experimental results

The evolution of calcium, magnesium, and sulfate concentrations differs as a function of initial mineralogy among the two brine–rock experiments and the two supercritical carbon dioxide–brine–rock experiments prior to injection of supercritical carbon dioxide. Calcium concentrations stabilize within the first 400 h of both the brine–Do–Cc–Anh–Py experiment (Fig. 3A) and the supercritical

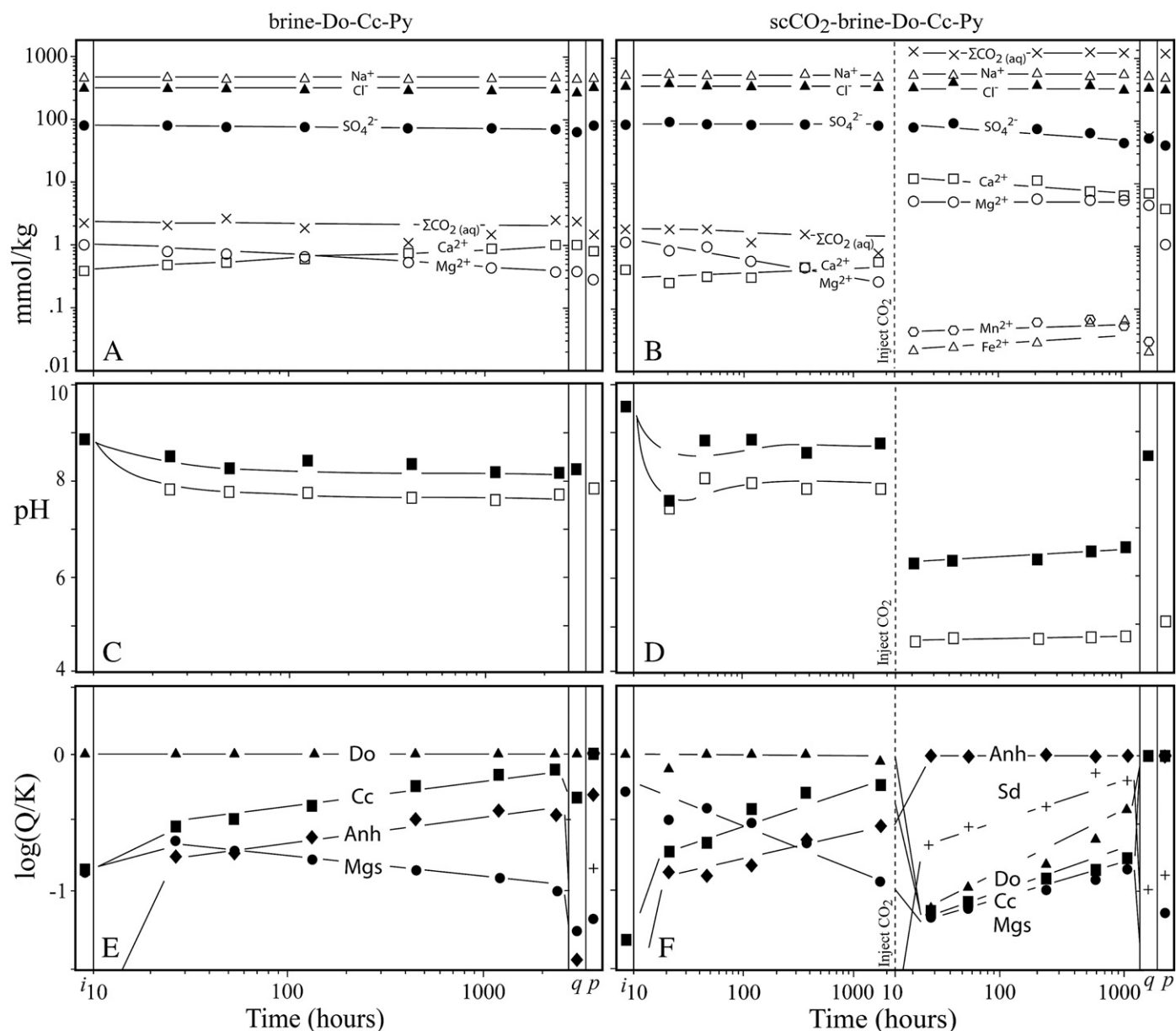


Fig. 4. Geochemistry of brine as a function of log time for the brine-Do-Cc-Py experiment (graphs in column on the left) and the scCO₂-brine-Do-Cc-Py experiment (graphs in column on the right). A) and B) Log concentration of Na (triangle), Ca (square), Mg (circle), Fe (triangle), Mn (hexagon), Cl (filled triangle), SO₄ (filled circle), and ΣCO₂ ('x'); C) and D) benchtop pH (filled square) and calculated in-situ pH (square); and E) and F) calculated saturation states of the minerals anhydrite (filled diamond), dolomite (filled triangle), calcite (filled square), siderite (Sd, crosses), and magnesite (Mgs, filled circles). Each graph also depicts the geochemistry of unreacted brine at 25 °C, 0.1 MPa (panel labeled *i*); the geochemistry of the brine at 25 °C, 0.1 MPa after termination of the experiment (panel labeled *q*); and the predicted equilibrium state of the brine at 110 °C, 25 MPa (panel labeled *p*).

carbon dioxide-brine-Do-Cc-Anh-Py experiment prior to injection (Fig. 3B). Magnesium and sulfate concentrations remain constant in the brine-Do-Cc-Anh-Py experiment and the supercritical carbon dioxide-brine-Do-Cc-Anh-Py experiment prior to injection. The stabilization of major element concentrations and in-situ pH in the two anhydrite-bearing experiments (Table 2 and Fig. 3) suggests that the brine achieved an approximate steady state controlled by the mineral assemblage.

Calcium concentrations steadily increase and magnesium and sulfate concentrations steadily decrease in the brine-Do-Cc-Py experiment (Fig. 4A) and the supercritical carbon dioxide-brine-Do-Cc-Py experiment prior to injection (Fig. 4B). These relationships suggest that the brine did not achieve a steady state.

Sodium and chloride concentrations in the brines remain constant throughout the duration of all four experiments (Figs. 3 and 4(A and

B) and Tables 2 and 3). Constant concentration of the conservative anion chloride in closed-system experiments such as ours indicates that the titanium reaction cells maintained their integrity for the duration of each experiment.

Injection of carbon dioxide produced significant changes in brine chemistry. Calcium and magnesium concentrations increase and sulfate concentrations decrease in the first sample collected after carbon dioxide was injected into both supercritical carbon dioxide-brine-rock experiments (Figs. 3B and 4B). Calcium and magnesium concentrations increased to approximately the same value in both experiments. Calcium and magnesium concentrations increased by approximately 3× and 5×, respectively, in the anhydrite-bearing experiment and by approximately 21× and 19×, respectively, in the experiment that did not initially contain anhydrite. Magnesium concentrations remain relatively constant for the duration of the

experiments whereas calcium and sulfate concentrations subsequently decrease in both experiments due to precipitation of anhydrite (Sections 3.4 and 3.5). Sulfate concentrations decreased by $2.1\times$ (46%) in the Do–Cc–Anh–Py experiment and by $1.7\times$ (58%) in the Do–Cc–Py experiment in the final sample collected before the experiments were terminated. Iron and manganese first appear in solution in concentrations of several hundredths of a millimole in the sample collected immediately after injection (Figs. 3B and 4B). Iron concentrations subsequently increase for the duration of both experiments. Manganese concentrations remain relatively constant in the Do–Cc–Anh–Py experiment but increase in the Do–Cc–Py experiment. Significant increase in calcium, magnesium, iron and manganese concentrations suggests that the minerals are dissolved by reaction with brine, a behavior consistent with the decrease of in-situ pH (Section 3.3) that accompanied injection of supercritical carbon dioxide and concomitant dissolution of carbon dioxide into the brine.

In both brine–rock experiments, concentrations of all of the ions in brine samples collected after the experiments were terminated (panel labeled “q” in Figs. 3A and 4A) were the same as concentrations in samples collected immediately prior to termination of the experiments. In contrast, dissolved calcium and sulfate concentrations increased in the samples of brine collected after the two supercritical carbon dioxide–brine–rock experiments were terminated (Figs. 3B and 4B). The increase in calcium and sulfate concentration is consistent with anhydrite dissolution during the termination process of degassing, depressurizing, and cooling. Concentrations of magnesium and manganese did not change due to the termination process in the Do–Cc–Anh–Py experiment but decreased in the Do–Cc–Py experiment by $0.1\times$ and $2.5\times$, respectively. Concentrations of iron decreased by approximately $5\times$ due to the termination process whereas concentrations of dissolved sodium and chloride did not change.

3.1.2. Predicted brine geochemistry

In this section we compare values predicted for the major elements (Section 2.5) to concentrations measured in the sample collected immediately before terminating each of the four experiments. Concentrations predicted for calcium, sulfate, and the conservative ions sodium and chloride in all four experiments compare favorably to measured values (panel labeled “p” in Figs. 3 and 4(A and B); Tables 2 and 3). Predictions for magnesium in both brine–rock experiments also compare favorably with measured values. In contrast, predictions for magnesium in both experiments injected with supercritical carbon dioxide are lower than the measured values.

3.2. Total dissolved inorganic carbon

3.2.1. Experimental results

Total dissolved inorganic carbon (DIC) concentrations stabilize within 50 h in the two brine–rock experiments and the two supercritical carbon dioxide–brine–rock experiments prior to injection (Figs. 3 and 4(A and B) and Tables 2 and 3). Total DIC concentrations increased by three orders of magnitude in the first sample collected after injection (Figs. 3B and 4B), from approximately 1 mmolal to 1 molal, and stabilized within 24 h after injection. Concentrations of total DIC decreased by approximately $20\times$ in the samples collected after the two supercritical carbon dioxide–brine–rock experiments were terminated.

3.2.2. Predicted total dissolved inorganic carbon

Predicted DIC values measured in both brine–rock experiments (1.2 to 1.4 mmolal) are similar to measured values of 1.1 to 2.7 mmolal (Tables 2 and 3). Somewhat larger amounts of DIC in many of the samples may be due to contamination of the experiment with atmospheric carbon dioxide during assembly, contamination of the samples with

atmospheric carbon dioxide, and/or larger uncertainties associated with the measurement of small amounts of carbon dioxide.

Predicted equilibrium concentrations of total DIC in both supercritical carbon dioxide–brine–rock experiments compare exceedingly well (<1% to 6%) to values measured in the sample collected immediately before terminating both of these experiments (Tables 2 and 3; panel labeled “p” in Figs. 3B and 4B). Agreement between predicted and measured DIC values in these experiments is due to the immiscible supercritical carbon dioxide maintaining carbon dioxide saturation in the brine.

3.3. pH

3.3.1. Experimental results

The pHs of unreacted brine in the brine–Do–Cc–Anh–Py experiment and the supercritical carbon dioxide–brine–Do–Cc–Anh–Py experiment are 8.6 and 9.8, respectively (measured at 25 °C, Table 2 and Figs. 3C and 3D). The difference between these pH values is attributed to pH changes in brine stored during the time interval between carrying out the two experiments. Calculated in-situ pH stabilizes within approximately 400 h in both of these experiments, to a value of approximately 7.3.

The pHs of unreacted brine in the brine–Do–Cc–Py experiment and the supercritical carbon dioxide–brine–Do–Cc–Py experiment are 8.9 and 9.6, respectively (measured at 25 °C, Table 3 and Figs. 4C and 4D). The difference between these pH values is also attributed to pH changes in brine stored during the time interval between carrying out the two experiments. Calculated in-situ pH of the brine–Do–Cc–Py experiment decreases throughout the duration of the experiment (Fig. 4C), consistent with changing calcium and magnesium in this experiment. An in-situ pH of 7.9 is calculated for the supercritical carbon dioxide–brine–Do–Cc–Py experiment before carbon dioxide is injected.

Injection of supercritical carbon dioxide into the experiments abruptly decreases pH (Figs. 3D and 4D). This pH decrease is consistent with dissolution of supercritical carbon dioxide into brine and subsequent formation and dissociation of carbonic acid. In-situ pH decreased by 2.5 and 3.3 pH units to 4.8 and 4.6 in the Do–Cc–Anh–Py and Do–Cc–Py experiments, respectively. In-situ pH remained at these values during the remainder of both experiments. These steady state in-situ pH values are similar to values calculated in published laboratory studies of supercritical carbon dioxide–water–rock interactions (Kaszuba et al., 2003; Kaszuba et al., 2005; Rosenbauer et al., 2005).

3.3.2. Predicted in-situ pH

In this section we compare predicted in-situ pH values (Section 2.5) to in-situ pH in the sample collected immediately before terminating each of the four experiments. In-situ pH in both brine–rock experiments is identical to predicted values (Tables 2 and 3; Figs. 3 and 4). In contrast, in-situ pHs in both experiments injected with supercritical carbon dioxide are 0.3 to 0.4 units lower than predicted values.

3.4. Saturation state

3.4.1. Saturation state calculated for the experiments

Dolomite is saturated and calcite is undersaturated in both of the brine–rock experiments and in both of the supercritical carbon dioxide–brine–rock experiments prior to injection (Figs. 3 and 4E and F). Magnesite and siderite precipitate in other experimental studies and in geochemical modeling studies that evaluate supercritical carbon dioxide–brine–rock interactions (Kaszuba et al., 2003; Xu et al., 2004; Kaszuba et al., 2005; Palandri et al., 2005; Zerai et al., 2006; Xu et al., 2007; Montes-Hernandez and Pironon, 2009). Magnesite and siderite were not part of the starting mineral assemblage in our

brine–rock experiments. Magnesite is undersaturated in our experiments whereas siderite does not plot on the saturation state diagrams because detectable quantities of aqueous iron are not present in the experiments.

Anhydrite is initially undersaturated but becomes saturated within 50 h in both the brine–Do–Cc–Anh–Py experiment and the supercritical carbon dioxide–brine–Do–Cc–Anh–Py experiment prior to injection. Anhydrite is undersaturated in both the brine–Do–Cc–Py experiment and the supercritical carbon dioxide–brine–Do–Cc–Py experiment prior to injection.

Pyrite and native sulfur plot off the scale of the saturation state diagrams. The saturation index of pyrite in all four experiments is approximately -160 prior to injection and -106 after injection. Native sulfur occurs in the Madison Limestone (Kaszuba et al., 2011) but was not part of the starting mineral assemblage in our experiments. The saturation index of native sulfur is approximately -71 prior to injection and -49 after injection.

Injection of carbon dioxide produced significant changes in the saturation state of the brines (Figs. 3F and 4F). Dolomite becomes undersaturated and calcite remains undersaturated in both supercritical carbon dioxide experiments. Dissolution of dolomite releases iron into the brine; siderite now plots on the diagrams and approaches, but never reaches, saturation. The saturation index of dolomite, calcite, and magnesite increases during the course of both supercritical carbon dioxide–brine–rock experiments. Anhydrite remains saturated in the supercritical carbon dioxide–brine–Do–Cc–Anh–Py experiment and becomes saturated in the supercritical carbon dioxide–brine–Do–Cc–Py experiment immediately after injection.

Brine recovered after the termination of both supercritical carbon dioxide–brine–rock experiments is saturated with respect to calcite and dolomite and undersaturated with respect to anhydrite (Figs. 3F and 4F). Siderite and magnesite remain undersaturated in these samples.

3.4.2. Predicted saturation state

Geochemical calculations predict that both brine–rock experiments will be saturated in dolomite, calcite and pyrite and undersaturated

in magnesite and siderite (Figs. 3E and 4E). Anhydrite is predicted to be saturated in the brine–Do–Cc–Anh–Py experiment but undersaturated in the brine–Do–Cc–Py experiment.

Geochemical calculations predict that both supercritical carbon dioxide–brine–rock experiments will be saturated in anhydrite, calcite, dolomite and pyrite and undersaturated in both siderite and magnesite (Fig. 3F and 4F). The predicted saturation indices for magnesite are lower than saturation indices that are calculated for both brine–rock experiments (Figs. 3E and 4E). Predicted saturation indices for both magnesite and siderite are significantly lower than values calculated for both supercritical carbon dioxide–brine–rock experiments (Figs. 3F and 4F).

3.5. Mineral dissolution textures and alteration assemblages

Mineral fragments were recovered from the reaction cell after each of the four experiments was terminated. Textures developed on these fragments were compared to textures of unreacted samples to evaluate reactions in the experiments.

Unreacted dolomite (Fig. 5A), calcite (Fig. 5C), and anhydrite surfaces (Fig. 6A) are smooth and planar. Minor dissolution steps develop on anhydrite (Fig. 6B) and to a much lesser extent on calcite in the brine–Do–Cc–Anh–Py experiment. In contrast, dissolution steps are more pronounced on calcite (Fig. 5D) in the brine–Do–Cc–Py experiment. Calcite and anhydrite dissolution textures in both brine–rock experiments developed because the brine was not perfectly saturated with the minerals in these experiments (Section 2.3).

Major dissolution textures develop on calcite in both supercritical carbon dioxide–brine–rock experiments (Fig. 5E and 5F). Minor dissolution textures developed on dolomite (Fig. 5B) and, to a lesser extent, pyrite. These calcite, dolomite and pyrite textures formed due to injection of supercritical carbon dioxide and developed in addition to the textures described in the previous paragraph. Large (up to 0.5 mm across) euhedral crystals of anhydrite precipitate following injection of supercritical carbon dioxide in both experiments (Figs. 6C and 6D).

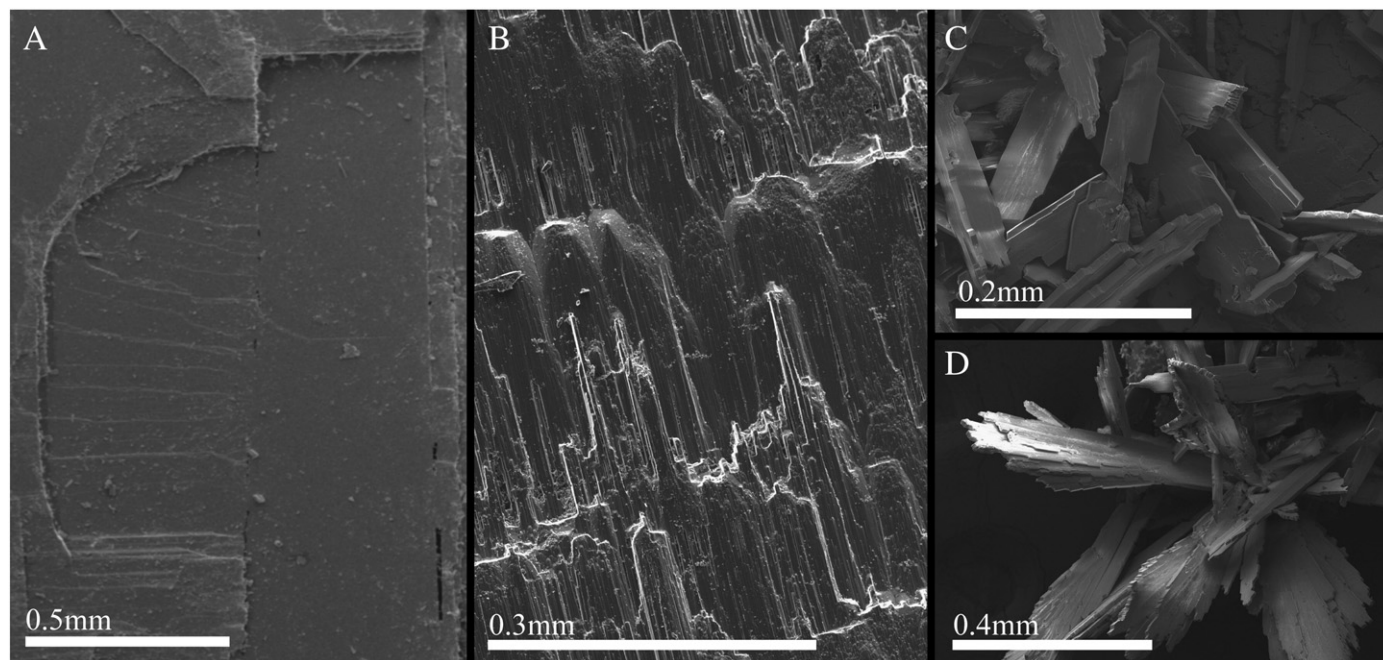


Fig. 5. Field emission scanning electron microscope (FE-SEM) micrographs of dolomite and calcite. Scale bars vary among the images. A) Unreacted dolomite. B) Dolomite recovered from the scCO_2 –brine–Do–Cc–Anh–Py experiment. Dissolution along cleavage planes is evident. C) Unreacted calcite. D) Calcite recovered from the brine–Do–Cc–Py experiment. E) and F) Calcite recovered from the scCO_2 –brine–Do–Cc–Anh–Py and scCO_2 –brine–Do–Cc–Py experiments, respectively. Major dissolution textures are evident in both images.

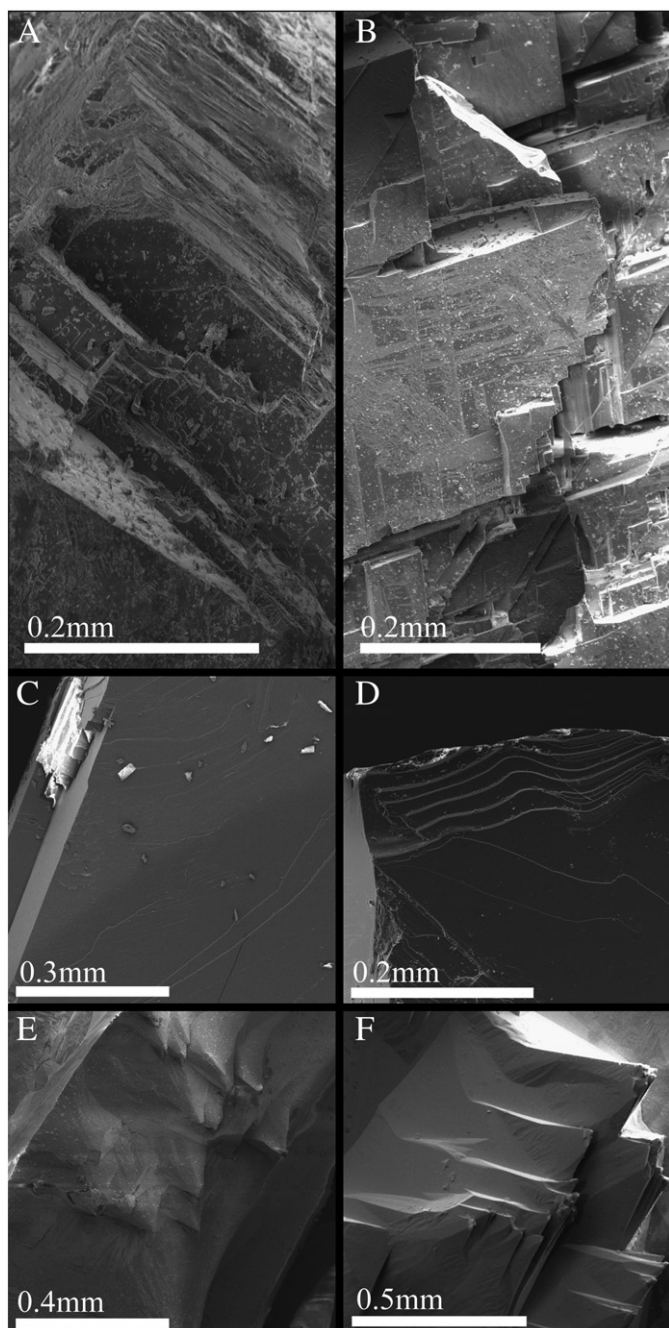


Fig. 6. FE-SEM micrographs of anhydrite. Scale bars vary among the images. A) Unreacted anhydrite. B) Anhydrite recovered from the brine-Do-Cc-Anh-Py experiment. Dissolution textures are evident. C) and D) Euhedral anhydrite crystals that precipitated in both the brine-scCO₂-Do-Cc-Anh-Py and the brine-scCO₂-Do-Cc-Py experiments, respectively.

4. Discussion

4.1. Geochemical predictions, experimental results, and the path to equilibrium

As described in Section 2.5, we calculated forward models to determine the equilibrium geochemical state to which each of the four experiments would theoretically evolve. Calculations for the brine-Do-Cc-Anh-Py experiment compare favorably with values measured at the conclusion of this experiment (Fig. 3), suggesting that this experiment approached equilibrium. This result is not surprising because the brine was synthesized to be saturated with the

minerals used in this experiment. Predictions for the brine-Do-Cc-Py experiment do not compare quite as well to experimentally-measured values because anhydrite is not part of the starting mineral assemblage. The brine evolved toward saturation with anhydrite (Fig. 4E), but the experiment was terminated before achieving anhydrite (and calcite) saturation. Comparing predictions to the geochemical evolution of both experiments reacted with supercritical carbon dioxide (Figs. 3, 4, and 7) suggests that these two experiments were terminated before achieving equilibrium. Prior to injection, these experiments approached equilibrium in the same fashion as their parallel brine-rock experiments. Injection of supercritical carbon dioxide disrupted paths to equilibrium and established paths to new equilibrium states. Both experiments progressed toward these new states; however, the experiments were terminated after approximately 1100 h and before attaining equilibrium with respect to pH, calcium and magnesium concentrations, and saturation state. In contrast, equilibrium with respect to anhydrite and aqueous sulfate was established approximately 24 h after injection.

4.2. Interactions among supercritical carbon dioxide, brine, and Madison Limestone in a natural carbon dioxide reservoir

4.2.1. The system CaO-CO₂-SO₄²⁻-H₂O

To understand the nature of interactions among supercritical carbon dioxide, brine, and Madison Limestone, we constructed two activity diagrams for the CaO-CO₂-SO₄²⁻-H₂O system, one for the Do-Cc-Anh-Py experiments (Fig. 7A) and a second for the Do-Cc-Py experiments (Fig. 7B). Stability fields for dolomite and anhydrite are plotted for: 1) conditions that existed immediately prior to injection of supercritical carbon dioxide, designated with solid phase boundaries; 2) conditions that existed after supercritical carbon dioxide was injected but immediately prior to terminating the experiment, designated with long dashed phase boundaries; and 3) predicted equilibrium conditions following injection of supercritical carbon dioxide, designated with short dashed phase boundaries (Figs. 7A and 7B). A stability field for calcite would emerge at the junction of the dolomite-aqueous stability fields (Figs. 7A and 7B) if the calcium activity in the experiments increased by 1.2 log units. For each of the aqueous samples collected in our experiments we plot log $a_{\text{HCO}_3^-}$ and log $a_{\text{SO}_4^{2-}}$ values in Fig. 7.

Samples collected from the brine-Do-Cc-Anh-Py experiment plot in a cluster in the dolomite stability field near the junction of the dolomite, anhydrite and aqueous stability fields (Fig. 7A). Samples collected from the supercritical carbon dioxide-brine-Do-Cc-Anh-Py experiment prior to injection also plot in this cluster. The data plot near but not on the anhydrite saturation boundary, consistent with minor anhydrite dissolution textures (Section 3.5) observed in both experiments. These dissolution textures are not produced by injection of supercritical carbon dioxide but from equilibration of brine and rock before supercritical carbon dioxide became part of the reactive system.

Samples collected from the brine-Do-Cc-Py experiment and the supercritical carbon dioxide-brine-Do-Cc-Py experiment plot in a cluster that straddles the boundary between the dolomite and aqueous stability fields (Fig. 7B). These experiments do not contain anhydrite in the starting mineral assemblage and are not saturated with anhydrite, thus the anhydrite stability field does not appear on Fig. 7B.

Injection of supercritical carbon dioxide into the Do-Cc-Anh-Py experiment shifts the junction of the dolomite, anhydrite, and aqueous stability fields to a higher value of log $a_{\text{HCO}_3^-}$ and a lower value of log $a_{\text{SO}_4^{2-}}$ (Fig. 7A). Brine samples from this experiment plot in the anhydrite stability field and close to the dolomite-anhydrite saturation boundary. Injection of supercritical carbon dioxide into the Do-Cc-Py experiment leads to the development of an anhydrite stability field (Fig. 7B). Brine samples from this experiment plot in this

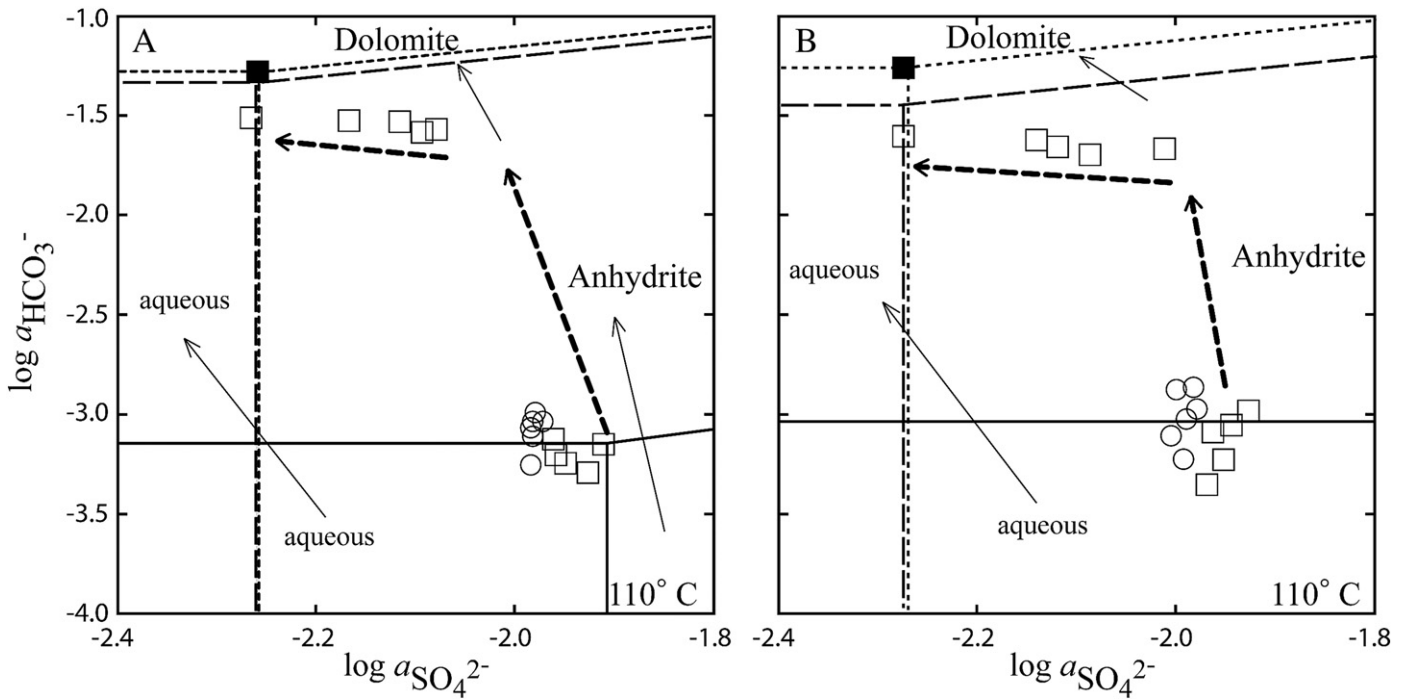


Fig. 7. Geochemical evolution of scCO_2 -brine-rock experiments in the $\text{CaO-CO}_2\text{-SO}_4^{2-}\text{-H}_2\text{O}$ system at 110°C . Stability fields for dolomite, anhydrite, and aqueous fluid at in-situ conditions prior to (solid lines) and after (long dashed lines) injection of scCO_2 are depicted. Stability fields predicted for equilibrium conditions in the scCO_2 -brine-rock experiments (short dashed lines, filled square) are also depicted. A) Diagram plotting $\log a_{\text{HCO}_3^-}$ versus $\log a_{\text{SO}_4^{2-}}$ for $\pm \text{scCO}_2$ -brine-Do-Cc-Anh-Py experiments. Aqueous samples are plotted for brine-Do-Cc-Anh-Py experiment (open circles) and scCO_2 -brine-Do-Cc-Anh-Py experiment (open squares). The temporal sequence of samples in the scCO_2 experiment defines a reaction path trajectory (bold dashed arrows) toward the dolomite saturation boundary. B) Diagram plotting $\log a_{\text{HCO}_3^-}$ versus $\log a_{\text{SO}_4^{2-}}$ for $\pm \text{scCO}_2$ -brine-Do-Cc-Py experiments. Aqueous samples are plotted for brine-Do-Cc-Py experiment (open circles) and scCO_2 -brine-Do-Cc-Py experiment (open squares). The temporal sequence of samples in the scCO_2 experiment defines a reaction path trajectory (bold dashed arrows) toward the aqueous stability field. Anhydrite field appears after injection of supercritical CO_2 .

anhydrite stability field and near the dolomite-anhydrite saturation boundary. Note that these samples plot approximately 0.1 $\log a_{\text{HCO}_3^-}$ units further away from the dolomite-anhydrite saturation boundary compared to samples in the supercritical carbon dioxide-brine-Do-Cc-Anh-Py experiment (Fig. 7A). The stability of anhydrite depicted in both diagrams is consistent with precipitation of euhedral anhydrite (Section 3.5 and Fig. 6C and D) and the decrease of calcium and sulfate concentrations in reacted brine (Section 3.1, Tables 2 and 3, and Figs. 3B and 4B).

The temporal sequence of samples in both experiments defines a reaction path of progressively decreasing $\log a_{\text{SO}_4^{2-}}$ at relatively constant $\log a_{\text{HCO}_3^-}$ values. In the supercritical carbon dioxide-brine-Do-Cc-Anh-Py experiment this reaction path defines a trajectory toward the dolomite saturation boundary (Fig. 7A). The last sample collected before the experiment was terminated plots on the junction of the dolomite, anhydrite and aqueous stability fields. In the supercritical carbon dioxide-brine-Do-Cc-Py experiment this reaction path defines a trajectory toward the aqueous stability field (Fig. 7B). The last sample collected before this experiment was terminated plots on the junction of the anhydrite and aqueous stability fields, just below the dolomite stability field.

4.2.2. Eh-pH

To further understand the nature of interactions in this multi-phase fluid-Madison Limestone system we constructed an Eh-pH diagram that includes all of the major sulfur-bearing minerals that are reacting in our experiments. Stability fields for minerals (anhydrite, pyrite, and native sulfur), aqueous sulfate, and hydrogen sulfide gas are plotted for aqueous conditions that existed immediately prior to injection of supercritical carbon dioxide (dashed phase boundaries) and termination of the experiment (solid phase boundaries) (Fig. 8). The relative size and hence importance of the mineral, aqueous, and gas stability fields change due to changes in brine chemistry

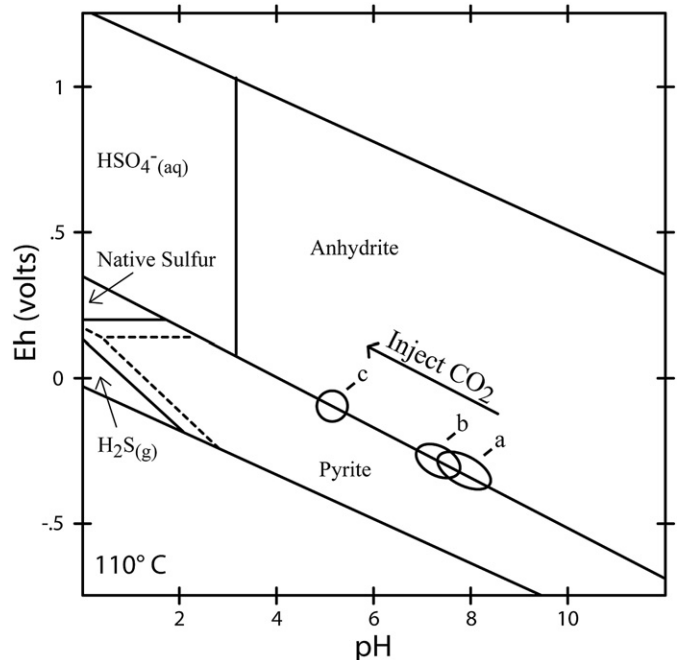


Fig. 8. Eh-pH diagram for iron-sulfur system showing stability fields of sulfur phases at 110°C . In-situ conditions immediately prior to injection of scCO_2 (dashed lines) and immediately prior to termination of the experiments (solid lines) are depicted. Aqueous samples from the brine-Do-Cc-Py experiment and the scCO_2 -brine-Do-Cc-Py experiment prior to injection of scCO_2 are plotted in the field labeled "a". Aqueous samples from the brine-Do-Cc-Anh-Py experiment and from the scCO_2 -brine-Do-Cc-Anh-Py experiment prior to injection of scCO_2 are plotted in the field labeled "b". Field "c" encompasses post-injection brine compositions from both scCO_2 experiments. Predicted equilibrium compositions also plot within the field labeled "c". The arrow represents the reaction pathway after injection of scCO_2 .

produced by injection of supercritical carbon dioxide. The size of the anhydrite stability field increases by the width of a line due to an increase in calcium activity created by dissolution of calcite and dolomite (Section 3.5). Calcite dissolution thus facilitates anhydrite precipitation. Iron was not initially present in the brine (Section 3.1) but is released into solution by dissolution of dolomite. The resulting increase in iron concentrations, from less than detection to 0.5 mmolal (Tables 2 and 3), increases the size of the pyrite stability field and simultaneously decreases the size of the hydrogen sulfide (gas) and native sulfur stability fields.

All samples from the brine–Do–Cc–Py experiment and the supercritical carbon dioxide–brine–Do–Cc–Py experiment prior to injection plot in the field labeled “a” in Fig. 8. Likewise, all samples from the brine–Do–Cc–Anh–Py experiment and from the supercritical carbon dioxide–brine–Do–Cc–Anh–Py experiment prior to injection plot in the field labeled “b” in Fig. 8. Both fields encompass samples at in-situ conditions (110 °C). Initial brine chemistries and quench samples are not plotted. Field “c” encompasses post-injection brine chemistries from both supercritical carbon dioxide experiments. Predicted equilibrium conditions also plot in the field labeled “c”. The arrow labeled “Inject CO₂” in Fig. 8 represents the reaction pathway taken by the system after injection of supercritical carbon dioxide, starting at the fields labeled “a” and “b” and ending at the field labeled “c”.

Samples collected from the brine Do–Cc–Py experiments (field a) exhibit an average pH of 7.7 and Eh of –0.32 V. Samples collected from the brine Do–Cc–Anh–Py experiments (field b) exhibit an average pH of 7.3 and Eh of –0.29 V. Injection of supercritical carbon dioxide decreased pH in both experiments and increased Eh in the former by 0.23 V and in the latter by 0.19 V, to an average Eh of –0.09 V in both experiments. The reaction path is confined to the saturation boundary between the anhydrite and pyrite stability fields, the mineral assemblage observed in the natural Madison Limestone carbon dioxide reservoir (Kaszuba et al., 2011), and moves toward the native sulfur and aqueous sulfate stability fields. Despite differences in the initial mineralogy of these experiments both reaction paths terminate at the same endpoint (field c). In this Eh–pH diagram, supercritical carbon dioxide exerts primary control on brine chemistry relative to the buffering capacity of the rock. This observation is consistent with features observed in the evolution of brine chemistry over time (Figs. 3 and 4).

4.3. Geochemical processes in the Madison Limestone carbon dioxide reservoir

The dolomite–calcite–anhydrite–pyrite mineral assemblage produced in the supercritical carbon dioxide–brine–rock experiments, as well as the reaction textures displayed by these minerals, is consistent with mineral assemblages and textures present in the Madison Limestone on the Moxa Arch (Fig. 2 and Kaszuba et al., 2011). The bulk mineralogy of the experiment did not change as a consequence of injection of supercritical carbon dioxide (Fig. 7A). Instead, dolomite, calcite, and anhydrite dissolve and subsequently reprecipitate or approach saturation. This finding is in agreement with prior studies of the Madison Limestone on the Moxa Arch showing that 1) carbonate and sulfate minerals are secondary precipitates filling pores and fractures (Kaszuba et al., 2011); and 2) no significant difference in porosity exists in Madison Limestone within and outside of the carbon dioxide reservoir (Thyne et al., 2010). Thus, mineral dissolution and re-precipitation textures record the emplacement of carbon dioxide as well as infiltration of aqueous fluids or diagenetic changes.

Supercritical carbon dioxide changes the balance between rock- and fluid-dominated reaction systems (Kaszuba and Janecky, 2009). Mineral reactions buffer the aqueous geochemistry of rock-dominated reaction systems such as deep brine formations (Langmuir, 1997). In contrast, the fluid predominantly controls the aqueous geochemistry of fluid-dominated systems, (e.g., shallow aquifers that are replenished by fresh water recharge). All of the experiments started as rock-

dominated systems (Section 2.3). The geochemical evolution (Figs. 3 and 4) and reaction pathways (Figs. 7 and 8) observed in our experiments agree with other experimental studies in which 1) injection of supercritical carbon dioxide changes the experiment from a rock- to a fluid-dominated reaction system (Kaszuba et al., 2003; Kaszuba et al., 2005); and 2) multiphase fluid (CO₂–H₂O) equilibria lower pH and assume control of acid-dominated reactions and related dissolution–precipitation reactions (Kaszuba and Janecky, 2009). Injection also displaces reaction pathways from mineral–fluid saturation boundaries and drive toward three-phase field junctions (Fig. 7). With time the mineral assemblage would reach these junctions and ultimately reassert geochemical control. If our experiments had continued for a longer period of time they would have attained thermodynamic equilibrium in the manner of the Madison Limestone carbon dioxide reservoir. We could have designed experiments with lower fluid–rock ratios to reduce the amount of time needed to attain equilibrium on laboratory time scales. However, our design balances duration of experiment and the actual attainment of equilibrium with the insight afforded by sampling intensity that defines reaction paths and clear trajectories toward equilibrium. Since our experiments are closed, well-defined systems and since none of the minerals is consumed by reaction, our choice of a modest fluid:rock ratio to maximize the mass of fluid available for sampling does not change the ultimate equilibrium state of these experiments. Thus, properly formulated and constrained equilibrium laboratory experiments can be useful for predicting the long-term fate of reactive carbon in a natural carbon dioxide reservoir as well as a sequestration scenario, even if complete equilibrium is not achieved on the laboratory scale.

4.4. The Madison Limestone as a natural analog for geologic co-sequestration of carbon dioxide and sulfur

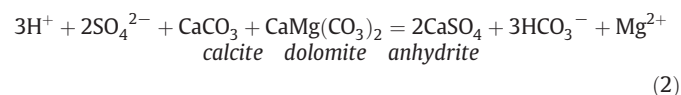
Our experimental results are consistent with the thermodynamic assessment performed by Kaszuba et al. (2011) for the Madison Limestone–brine–carbon dioxide system. Those theoretical predictions agree with our experimental observations that emplacement of carbon dioxide decreases pH and increases Eh. Both thermodynamically predicted and experimentally observed reaction pathways lay on the pyrite–anhydrite saturation boundary of an Eh–pH diagram, which is the mineral assemblage observed in the Madison Limestone carbon dioxide reservoir.

Disproportionation of sulfur dioxide to sulfuric acid and aqueous hydrogen sulfide is the predominant reaction in water–rock systems spanning a wide range of geochemical conditions (Holland, 1965; Getahun et al., 1996; Symonds et al., 2001), including the geochemical conditions of the Madison Limestone (Kaszuba et al., 2011):



This reaction is also believed to be the predominant reaction for sulfur dioxide in geologic carbon sequestration scenarios (Palandri and Kharaka, 2005; Palandri et al., 2005; Xu et al., 2007).

By starting with aqueous sulfate, our experiments probe supercritical carbon dioxide reactions with a brine–rock system in which sulfur dioxide has produced sulfuric acid (Eq. 1) and, with subsequent dissociation, aqueous sulfate. Injection of supercritical carbon dioxide precipitates anhydrite in our experiments (Figs. 6D and 7B) with the overall reaction.



consistent with the observed mineralogy of the Madison Limestone (Fig. 2). Anhydrite precipitation provides a mineral trap for sulfur

and decreases aqueous sulfate activity, ultimately leading to carbonate re-precipitation and mineralization of carbon (Fig. 7). Thus our experiments support the hypothesis that the Madison Limestone on the Moxa Arch is a natural analog for geologic carbon–sulfur co-sequestration.

5. Conclusions and recommendations for future work

This experimental investigation evaluates multi-phase (CO₂–H₂O)–brine–rock reactions and processes in a sulfur-rich natural carbon dioxide reservoir. It also tests the hypothesis that the Madison Limestone on the Moxa Arch is a natural analog for geologic carbon–sulfur co-sequestration. The following are concluded from this investigation:

- 1) The dolomite–calcite–anhydrite mineral assemblage and reaction textures produced in supercritical carbon dioxide–brine–rock experiments are consistent with mineral assemblages and textures present in the natural carbon dioxide reservoir of the Madison Limestone on the Moxa Arch. These results are consistent with the thermodynamic assessment for the Madison Limestone–brine system performed by Kaszuba et al. (2011).
- 2) Injection of supercritical carbon dioxide into the experiments decreases pH, increases Eh, and drives reaction pathways along the pyrite–anhydrite saturation boundary of an Eh–pH diagram. The mineral assemblage produced in the experiments, and by analogy in the natural system, does not change in response to emplacement of supercritical carbon dioxide. Instead, minerals dissolve, mobilize and re-precipitate. Mineral dissolution and re-precipitation textures observed in the Madison Limestone on the Moxa Arch could record emplacement of carbon dioxide as opposed to infiltration of aqueous fluids or diagenetic changes.
- 3) Anhydrite precipitates in response to injection of supercritical carbon dioxide and provides a mineral trap for sulfur. Anhydrite precipitation decreases aqueous sulfate activity, ultimately leading to carbonate re-precipitation and thus mineralization of carbon. The Madison Limestone on the Moxa Arch is a natural analog for geologic carbon–sulfur co-sequestration.

We recommend the following as important directions for future scientific research:

- 1) Evaluate reactions and processes in an experimental carbonate reservoir system containing the accessory silicate minerals (quartz, feldspar, clay, and analcime) that are also present in the Madison Limestone.
- 2) Experimentally evaluate other lithologies that naturally store carbon dioxide on the Moxa Arch, including siliciclastic rocks such as the Weber Sandstone.
- 3) Emulate an actual co-injection scenario by incorporating sulfur dioxide into injected supercritical carbon dioxide.

Acknowledgments

Acknowledgment is made to the Donors of the American Chemical Society Petroleum Research Fund for partial support of this research. This project was also partially supported by a DOE Fossil Energy grant DE-NT004730 to Kaszuba and Thyne, an SER grant WYDEQ49811KAS to Kaszuba, and an SER Graduate Assistantship to Chopping. John Kaszuba's work was also supported by the UW School of Energy Resources. We acknowledge The Laboratory for Environmental and Geological Studies (LEGS) at the University of Colorado, particularly Fredrick G. Luiszer, for aqueous analyses. We thank Susan Swapp and Norbert Swoboda-Colberg for assistance with XRD and SEM analyses and Kellie Antrobus for performing BET measurements at the University of Wyoming. Curtis Chopping thanks John Boyd, Brandon Overstreet, Virginia Marcon, Caroline Lo Ré, and especially Mary

Kate McCarney for help in the lab. Curtis Chopping also thanks Susan Swapp for her training, teaching and use of analytical equipment, but especially for her unwavering belief in his abilities and ambition to further his education with graduate studies. Curtis Chopping was primarily responsible for the experimental, analytical, and computational works presented in this paper. John Kaszuba was responsible for overall mentorship. Both authors shared in the manuscript preparation.

References

- Allis, R., et al., 2001. Natural CO₂ reservoirs on the Colorado Plateau and Southern Rocky Mountains: candidates for CO₂ sequestration. Proc. Natl. Conf. Carbon Sequestration.
- Bethke, C.M., Yeakel, S., 2009. The Geochemist's Workbench Release 8.0: Reaction Modeling Guide. University of Illinois, Champaign, Illinois. 84 pp.
- Breit, G.N., Skinner, C., 2002. USGS Produced Waters Database. US Geological Survey.
- Budai, J.M., Lohmann, K.C., Wilson, J.L., 1987. Dolomitization of the Madison Group, Wyoming and Utah Overthrust Belt. AAPG Bulletin 71 (8), 909–924.
- De Bruin, R.H., 1991. Wyoming's Carbon Dioxide Resources. OFR 91-6 Wyoming State Geological Survey.
- Duan, Z.H., Sun, R., Zhu, C., Chou, L.M., 2006. An improved model for the calculation of CO₂ solubility in aqueous solutions containing Na⁺, K⁺, Ca²⁺, Mg²⁺, Cl⁻, and SO₄²⁻. Marine Chemistry 98 (2–4), 131–139.
- Getahun, A., Reed, M.H., Symonds, R., 1996. Mount St Augustine volcano fumarole wall rock alteration: mineralogy, zoning, composition and numerical models of its formation process. Journal of Volcanology and Geothermal Research 71 (2–4), 73–107.
- Gilfillan, S.M., et al., 2008. The noble gas geochemistry of natural CO₂ gas reservoirs from the Colorado Plateau and Rocky Mountain provinces, USA. Geochimica et Cosmochimica Acta 72 (4), 1174–1198.
- Gunter, W.D., Wiwchar, B., Perkins, E.H., 1997. Aquifer disposal of CO₂-rich greenhouse gases: extension of the time scale of experiment for CO₂-sequestering reactions by geochemical modelling. Mineralogy and Petrology 59 (1–2), 121–140.
- Holland, H.D., 1965. Some applications of thermochemical data to problems of ore deposits II. Mineral assemblages and the composition of ore forming fluids. Economic Geology 60 (6), 1101–1166.
- Huffmann, E., 1977. Performance of a new automatic carbon dioxide coulometer. Microchemical Journal 22 (4), 567–573.
- Kaszuba, J.P., Janecky, D.R., 2009. Geochemical impacts of sequestering carbon dioxide in brine formations. In: McPherson, B., Sundquist, E. (Eds.), Carbon Sequestration and Its Role in the Global Carbon Cycle. Geophysical Monograph Series. American Geophysical Union, Washington, DC, pp. 239–247.
- Kaszuba, J.P., Janecky, D.R., Snow, M.G., 2003. Carbon dioxide reaction processes in a model brine aquifer at 200 °C and 200 bars: implications for geologic sequestration of carbon. Applied Geochemistry 18 (7), 1065–1080.
- Kaszuba, J.P., Janecky, D.R., Snow, M.G., 2005. Experimental evaluation of mixed fluid reactions between supercritical carbon dioxide and NaCl brine: relevance to the integrity of a geologic carbon repository. Chemical Geology 217 (3–4), 277–293.
- Kaszuba, J.P., Navarre-Sitchler, A., Thyne, G., Chopping, C., Meuzelaar, T., 2011. Supercritical carbon dioxide and sulfur in the Madison Limestone: a natural analogue in Southwest Wyoming for geologic carbon–sulfur co-sequestration. Earth and Planetary Science Letters 309, 131–140.
- Kraig, D.H., Wilschko, D.V., Spang, J.H., 1987. Interaction of basement uplift and thin-skinned thrusting, Moxa arch and the Western Overthrust Belt, Wyoming – a hypothesis. Geological Society of America Bulletin 99 (5), 654–662.
- Langmuir, D., 1997. Aqueous Environmental Geochemistry. Prentice Hall, Upper Saddle River, New Jersey. 600 pp.
- Lynds, R., Campbell-Stone, E., Becker, T.P., Frost, C.D., 2010. Stratigraphic evaluation of reservoir and seal in a natural CO₂ field: Lower Paleozoic, Moxa Arch, southwest Wyoming. Rocky Mountain Geology 45 (2), 113–132.
- Montes-Hernandez, G., Pironon, J., 2009. Hematite and iron carbonate precipitation-coexistence at the iron–montmorillonite–salt solution–CO₂ interfaces under high gas pressure at 150 °C. Applied Clay Science 45 (4), 194–200.
- Moore, J., Adams, M., Allis, R., Lutz, S., Rauzi, S., 2005. Mineralogical and geochemical consequences of the long-term presence of CO₂ in natural reservoirs: an example from the Springerville–St. Johns Field, Arizona, and New Mexico, USA. Chemical Geology 217 (3–4), 365–385.
- Newell, D.L., Kaszuba, J.P., Viswanathan, H.S., Pawar, R.J., Carpenter, T., 2008. Significance of carbonate buffers in natural waters reacting with supercritical CO₂: implications for monitoring, measuring and verification (MMV) of geologic carbon sequestration. Geophysical Research Letters 35 (23), 5.
- Palandri, J.L., Kharaka, Y.K., 2005. Ferric iron-bearing sediments as a mineral trap for CO₂ sequestration: iron reduction using sulfur-bearing waste gas. Chemical Geology 217 (3–4), 351–364.
- Palandri, J.L., Rosenbauer, R.J., Kharaka, Y.K., 2005. Ferric iron in sediments as a novel CO₂ mineral trap: CO₂–SO₂ reaction with hematite. Applied Geochemistry 20, 2038–2048.
- Pearce, J.M., et al., 1996. Natural occurrences as analogues for the geological disposal of carbon dioxide. Energy Conversion and Management 37 (6–8), 1123–1128.
- Rosenbauer, R.J., Koksalan, T., Palandri, J.L., 2005. Experimental investigation of CO₂–brine–rock interactions at elevated temperature and pressure: implications for

- CO₂ sequestration in deep-saline aquifers. *Fuel Processing Technology* 86, 1581–1597.
- Seyfried Jr., W.E., Janecky, D.R., Berndt, M.E., 1987. Rocking autoclaves for hydrothermal experiments. II. The flexible reaction-cell system. In: Ulmer, G.C., Barnes, H.L. (Eds.), *Hydrothermal Experimental Techniques*. John Wiley & Sons, New York, pp. 216–239.
- Shyu, G.S., Hanif, N.S.M., Hall, K.R., Eubank, P.T., 1997. Carbon dioxide–water phase equilibria results from the Wong–Sandler combining rules. *Fluid Phase Equilibria* 130 (1–2), 73–85.
- Smith, M.S., Sharma, S., Wyckoff, T.B., Frost, C.D., 2010. Baseline geochemical characterization of potential receiving reservoirs for carbon dioxide in the Greater Green River Basin, Wyoming. *Rocky Mountain Geology* 45 (2), 93–111.
- Span, R., Wagner, W., 1996. A new equation of state for carbon dioxide covering the fluid region from the triple-point temperature to 1100 K at pressures up to 800 MPa. *Journal of Physical and Chemical Reference Data* 25 (6), 1509–1596.
- Stevens, S.H., Pearce, J.M., Rigg, A.A.J., 2001. Natural analogs for geologic storage of CO₂: an integrated global research program. *Proc. Natl. Conf. Carbon Sequestration*. National Energy Technology Laboratory, US Department of Energy, Washington, D.C.
- Stilwell, D.P., 1989. CO₂ resources of the Moxa Arch and the Madison Reservoir. *Wyo. Geol. Assoc. 40th Annu. Field Conf.*, pp. 105–115.
- Symonds, R.B., Gerlach, T.M., Reed, M.H., 2001. Magmatic gas scrubbing: implications for volcano monitoring. *Journal of Volcanology and Geothermal Research* 108 (1–4), 303–341.
- Takenouchi, S., Kennedy, G.C., 1964. The binary system H₂O–CO₂ at high temperatures and pressures. *American Journal of Science* 262, 1055–1074.
- Thyne, G., Tomasso, M., Bywater-Reyes, S.V., Budd, D.A., Reyes, B.M., 2010. Characterization of porosity and permeability for CO₂ sequestration models in the Mississippian Madison Group, Moxa Arch-La Barge Platform, southwestern Wyoming. *Rocky Mountain Geology* 45, 133–150.
- Wyoming Oil and Gas Conservation Commission, 2009. Database. <http://wogcc.state.wy.us/> (last accessed September, 2009).
- Xu, T.F., Apps, J.A., Pruess, K., 2004. Numerical simulation of CO₂ disposal by mineral trapping in deep aquifers. *Applied Geochemistry* 19, 917–936.
- Xu, T.F., Apps, J.A., Pruess, K., Yamamoto, H., 2007. Numerical modeling of injection and mineral trapping of CO₂ with H₂S and SO₂ in a sandstone formation. *Chemical Geology* 242 (3–4), 319–346.
- Zerai, B., Saylor, B.Z., Matisoff, G., 2006. Computer simulation of CO₂ trapped through mineral precipitation in the Rose Run Sandstone, Ohio. *Applied Geochemistry* 21 (2), 223–240.